Available online at www.sciencedirect.com
ScienceDirect
Journal of the European Ceramic Society 31 (2011) 339–350
www.elsevier.com/locate/jeurceramsoc

Relationship between microstructure and abrasive wear resistance of Al_2O_3–$FeAl_2O_4$ nanocomposites produced via solid-state precipitation

Amartya Mukhopadhyay, Richard I. Todd *

Department of Materials, University of Oxford, Oxford OX1 3PH, UK

Received 6 August 2010; received in revised form 20 September 2010; accepted 4 October 2010

Abstract

The work investigates the correlation between the microstructure and wear behaviour of novel Al_2O_3–$FeAl_2O_4$ nanocomposites, developed by precipitation of $FeAl_2O_4$ particles through reduction aging of Al_2O_3–10 wt.% Fe_2O_3 solid solutions in N_2/4%H_2. Reduction aging at 1450 °C for 10 and 20 h resulted in considerable improvements in abrasive wear resistance. The nanocomposites developed from solid solutions doped additionally with ~250 ppm of Y_2O_3 contained finer intergranular second phase particles (by a factor of ~2) and showed further improvements in the wear resistance. Doped nanocomposites reduction aged for 20 h at 1450 °C exhibited the minimum wear rate (reduced by a factor of ~2.5 with respect to monolithic Al_2O_3). The suppression of fracture-induced surface pullout in the presence of intragranular nanosized second phase particles was the major factor responsible for the improved wear resistance of the nanocomposites with respect to monolithic alumina; microstructures without these intragranular nanoparticles showed no improvement. Higher aging temperature led to the presence of coarse (>2 μm) intergranular $FeAl_2O_4$ particles which had a detrimental effect on the wear resistance.

Keywords: Nanocomposite; Aging; Microstructure; Wear resistance

1. Introduction

Al_2O_3–matrix nanocomposites[1–9] exhibit superior mechanical and tribological properties to those of single phase alumina but processing difficulties have hindered their commercial application. The difficulties arise mainly from the mixed powder processing route that is commonly used. The incorporation of refractory, covalent nanoparticles such as SiC severely inhibits sintering.[2–4,8,9] Although pressureless sintering is possible with low volume fractions of SiC through the use of sintering aids,[10,11] the available processing window is limited. The more general solution has been to use pressure assisted sintering techniques, such as hot pressing and spark plasma sintering.[1–9] However, such techniques possess serious drawbacks with respect to mass scale commercial productions because as well as being very expensive, they are not suitable for continuous batch production and severely limit the shape and size of the components that can be produced.[2,3,12–14] When less refractory, oxide nanoparticles are incorporated into the powder mixture, pressureless sintering is feasible but the particles tend to coarsen beyond the nanosized regime and adhere to the grain boundaries.

To avoid these problems, an alternative to mixed powder processing has been developed in which the material is first sintered as a solid solution of Fe_2O_3 in Al_2O_3 and then $FeAl_2O_4$ nanoparticles are precipitated from the matrix by reduction of the dissolved Fe^{3+} cations.[12–15] This avoids both the inhibition of sintering by refractory second phases and the coarsening of oxide phases and may allow commercial exploitation of these promising materials.

Tribological applications encompass one of the major commercial uses of Al_2O_3, and Al_2O_3/SiC nanocomposites have been reported to possess much better resistance to severe wear than monolithic Al_2O_3.[2,3,5–7] The present work therefore investigates the abrasive wear resistance of the Al_2O_3–$FeAl_2O_4$ nanocomposites to establish whether similar advantages are possible in this system. The effects of different heat treatment schedules and Y_2O_3-doping on the wear resistance have been

* Corresponding author. Tel.: +44 1865 273718; fax: +44 1865 273783.
E-mail address: richard.todd@materials.ox.ac.uk (R.I. Todd).

0955-2219/$ – see front matter © 2010 Elsevier Ltd. All rights reserved.
doi:10.1016/j.jeurceramsoc.2010.10.014

investigated in detail and analysed in terms of the microstructural developments.

2. Experimental procedure

2.1. Processing and microstructure

α-Al_2O_3 powder (99.995% purity; AKP50, Sumitomo, Japan) with median particle size ~0.2 μm was used as the starting material for the matrix (Al_2O_3). Fe^{3+} and Y^{3+} were incorporated by adding solutions of $Fe(NO_3)_3{\cdot}9H_2O$ and $Y(NO_3)_3{\cdot}6H_2O$ (Sigma Aldrich, UK, purity >98%) in ethanol to the alumina slurries. Pure alumina slurries were also made for comparison. All the slurries, which also contained ~250 ppm of MgO,[16] were ball milled for 24 h in bottles made of polyethylene, using high purity (99.99%) alumina balls. After ball milling, the slurries were dried on a hot plate with a magnetic stirrer and ground in an Al_2O_3 mortar and pestle. Green compacts were produced by uniaxial cold pressing of the powders into 10 mm discs at 100 MPa, which were then pressurelessly sintered at 1450 °C for 5 h in air. After sintering, the samples were 'quenched' by pushing them immediately to the end of the furnace tube using an alumina rod. The Al_2O_3 samples containing 10 wt.% Fe_2O_3, will henceforth be referred to as 'A10F' and the samples additionally doped with Y_2O_3 (~250 ppm by weight) will be referred to as A10FY. The supersaturated solid solutions were then aged in a tube furnace with capped ends in a flowing N_2 + 4% H_2 forming gas mixture at 1450 °C and 1550 °C for different durations (0–20 h). Aging for 0 h indicates that the furnace was ramped up to the aging temperature and then the specimen was quenched immediately. More details about the processing are given in previous reports.[12–14] Although several components of the current processing route are not conducive to commercial production (e.g. the use of high purity alumina, ethanol as a dispersion medium, quenching of the specimens) these were included for scientific reasons during the development of these materials and it is anticipated that they can be dispensed with in practice.

For phase identification and microstructural characterization, the samples were ground and polished using diamond slurries in order to remove the external surfaces and produce optically reflective ceramographic surfaces representative of the sample cores. X-ray diffraction (XRD; Philips, Netherlands) was performed using Cu K_α radiation at a collection rate of 3°/min. The microstructures of all the polished surfaces were observed using a field emission scanning electron microscope (JEOL 6500F) operated at 20 kV. Sample preparation for transmission electron microscope (TEM) observations involved mechanical thinning of 3 mm discs, followed by ion-milling to electron transparency in a Gatan Duo Mill (5 kV). Observations were performed using a 200 kV JEOL 2000FX TEM, equipped with an EDS system.

2.2. Abrasive wear and indentation polish tests

A standard abrasive wear test, based on the use of a load-controlled grinding/polishing machine (MOTOPOL 2000, Buehler, UK) under standard conditions, was used to investigate the wear resistance of the materials. All the samples were in the form of pellets of 10 mm diameter and 3 mm thickness. The samples were attached using cyanoacrylate adhesive to resin cylinders (i.e. dummy metallographic specimens) in the standard carousel for metallographic preparation. The grinding was conducted using a 305 mm diameter resin-bonded alumina plate (Kemet, UK) with an oil-based suspension of 45 μm diamond abrasive. The specimens were ground for 4 min at 350 rpm rotation speed of the grinding plate and a force of 22.2 N per sample. This set up has been extensively used in our group for investigating the abrasive wear behaviour of Al_2O_3–SiC nanocomposites and has been shown to be reproducible.[5,6]

The mass loss during the test (Δm) was determined by weighing the specimens before and after each test. The wear rate (v) was defined as;

$$v = \frac{\Delta m}{\rho A t} \quad (1)$$

where A is the contact area, t is the testing time and ρ is the density of the material. The wear rate can be viewed as the velocity with which the surface recedes, or equivalently, the volume of material removed per unit contact area per unit time. Following initial bedding in, at least four of these standard tests were performed for each material. The worn surfaces of the different samples were observed in a SEM (JEOL 6500F). Prior to SEM observations, the worn samples were cleaned in an ultrasonic bath using ethanol. Area fractions of pullout and pullout diameter caused by brittle fracture were measured by linear intercepts with lines in a grid on SEM micrographs.[5,6]

Vickers indentations were made using 5 kg load on the polished surfaces of the specimens in order both to measure the hardness, and then to investigate crack initiation by plastic deformation.[6] The indented surfaces were subsequently polished with 1 μm diamond paste on a soft cloth using the automated grinding polishing machine (MOTOPOL 2000, Buehler, UK) until only the lower tip of the original indentation remained. In order to observe the presence of cracking that might have occurred beneath the indentations during polishing, the as polished surfaces near the residual indents were examined in the SEM (JEOL 6500F).

3. Results

3.1. Microstructural development, fracture surfaces and hardness

X-ray diffraction, SEM and TEM observations confirmed the development of single phase solid solutions of Al_2O_3–10 wt.% Fe_2O_3 (A10F and A10FY) possessing average grain sizes of ~3 μm after sintering, which was similar to that of the pure Al_2O_3. However, a few grains in the solid solutions showed anisotropic growth, whereas all the grains in the monolithic Al_2O_3 were equiaxed. On aging of the solid solutions in reducing atmosphere (N_2 + 4% H_2) at 1450 °C and 1550 °C, $FeAl_2O_4$ was precipitated as second phase particles due to reduction of dissolved Fe^{3+} to Fe^{2+}. The $FeAl_2O_4$ particles initially appeared only along the matrix grain boundaries and triple points (after

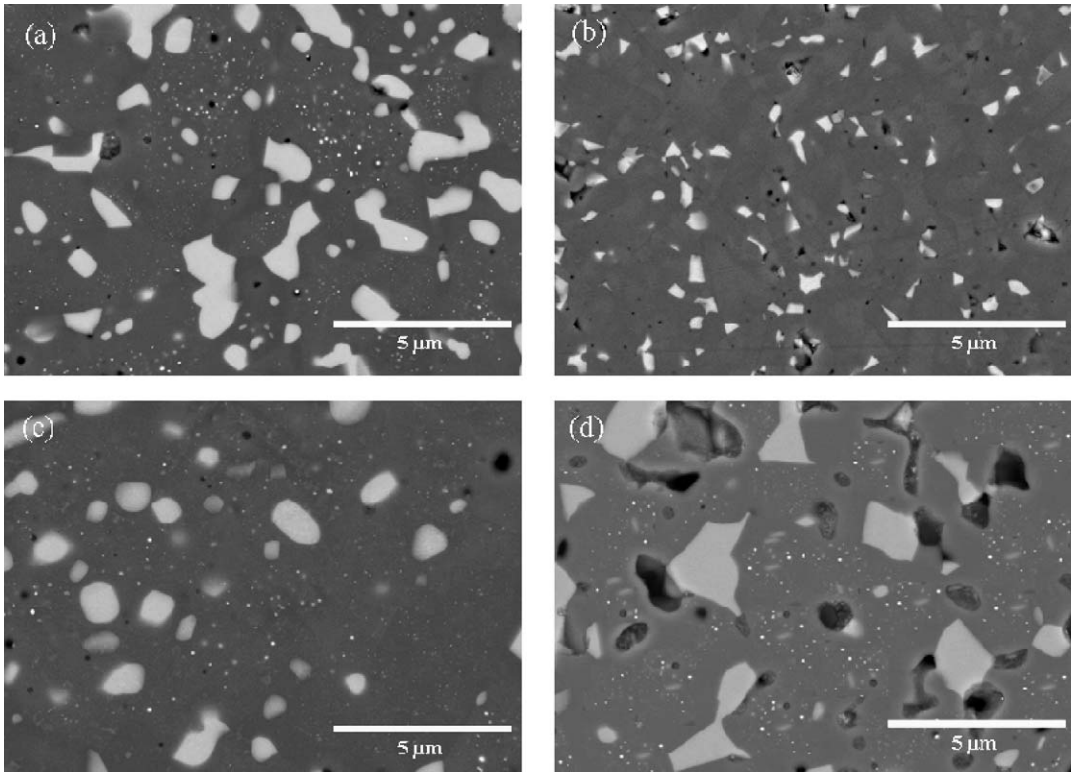

Fig. 1. Back scattered SEM (BSE-SEM) images showing bulk microstructural development on aging of (a) A10F solid solution (Y_2O_3-free) 1450 °C for 20 h; (b)–(d) A10FY solid solution (Y_2O_3-doped) and aged for (b) 1450 °C for 0 h; (c) 1450 °C for 20 h and (d) 1550 °C for 5 h.

0–5 h of aging), with intragranular particles ($FeAl_2O_4$) being precipitated on further increasing the aging duration to 10 h or more (Fig. 1). During aging of the Y_2O_3-free solid solution (A10F) at 1450 °C the intergranular particles initially appeared as micron sized particles and grew to a size >2 μm after aging for 20 h (Fig. 1a). The grain boundary precipitates in the Y_2O_3-doped solid solution (A10FY) were much finer, appearing initially as sub-micron particles and growing to a size of ~1 μm on aging at 1450 °C for 20 h (Fig. 1b). For a given aging time at 1450 °C, the addition of Y_2O_3 was found to reduce the size of the grain boundary precipitates by approximately a factor of 2, as has been reported previously.[13] This is presumed to be because Y_2O_3 is known to reduce the grain boundary diffusivity of alumina.[17–19] In contrast to the coarser intergranular particles, the intragranular $FeAl_2O_4$ particles were in the nanosized regime (<100 nm) even on aging for 20 h at 1450 °C (Fig. 1a and c). There was no effect of Y_2O_3-doping on the sizes of the intragranular particles but it did lead to the precipitation of a greater number of intragranular particles than in the Y_2O_3-free material aged for a given duration at 1450 °C.[13]

Much coarser intergranular $FeAl_2O_4$ particles (~3 μm) were formed even during the initial stages of aging at the higher temperature of 1550 °C. This was followed by extremely rapid growth during continued aging so that after just 5 h of aging at 1550 °C a coarse and inter-connected network of intergranular $FeAl_2O_4$ was formed (Fig. 1d). Considerable pullout of these coarse intergranular particles occurred during metallographic polishing. The addition of Y_2O_3 did not have any apparent effect on the sizes of the intergranular particles precipitated at 1550 °C. However, the $FeAl_2O_4$ particles that were precipitated within the matrix grains maintained their nanosized dimensions during aging at 1550 °C. More details concerning the microstructural development have been presented previously.[12–14]

TEM observations showed the presence of a high density of genuinely nano-scale $FeAl_2O_4$ particles inside the matrix grains (Fig. 2). Occasionally holes (~2 μm in size) were observed along the boundaries or triple point corners of the matrix grains in the foils developed from the nanocomposites obtained on aging A10F for 20 h (Fig. 2a). The holes appear to have been formed due to the coarser intergranular particles falling out during the TEM sample preparation. These were not observed for the Y_2O_3-doped nanocomposites (Fig. 2b).

The fracture mode of monolithic Al_2O_3, A10F and A10FY solid solutions was intergranular. The composites developed by aging for 0 h at both aging temperatures, in which only grain boundary precipitates were present, also exhibited mainly intergranular fracture (Fig. 3a). By contrast, the nanocomposites developed on aging for longer durations (10 and 20 h), in which nanosized particles were present within the grains, fractured in the transgranular mode (Fig. 3b).

The room temperature Vickers hardness values (H_v) are presented in Table 1. The solid solutions were less hard than pure alumina, but aging generally caused the hardness to increase towards the level of pure alumina. This has previously been attributed to the resulting removal of Fe^{3+} from solid solution.[13] However, a considerable reduction in hardness was observed on aging at the higher temperature of 1550 °C.

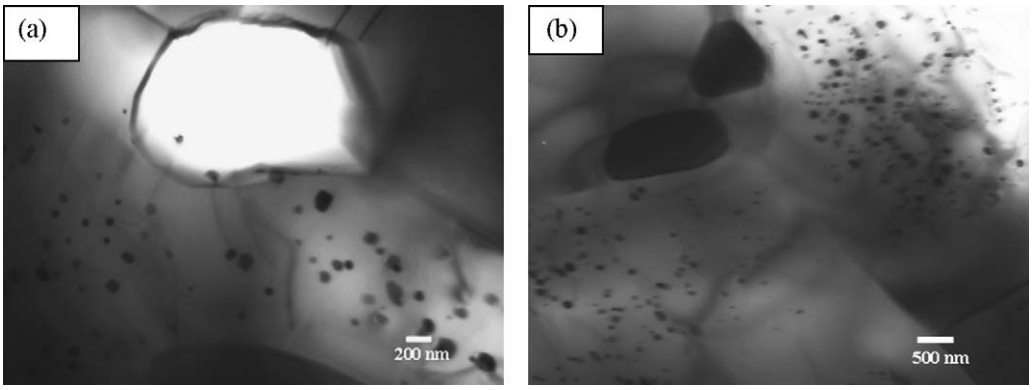

Fig. 2. Bright field TEM micrographs showing microstructural development on reduction aging at 1450 °C for 20 h of (a) A10F solid solution, showing the presence of hole left along the matrix grain boundary possibly due to fall out of a coarser intergranular particle during TEM sample preparation and (b) A10FY solid solution revealing the presence of comparatively fine second phase particles along the matrix grain boundaries and a high volume fraction of fine precipitates within the grains.

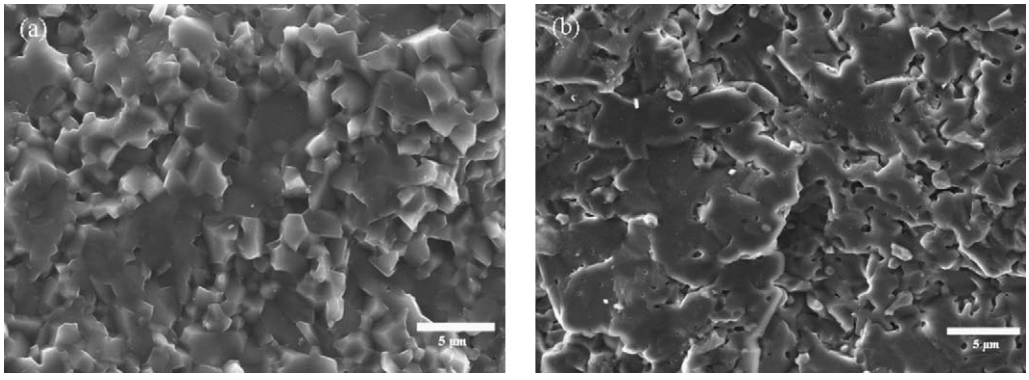

Fig. 3. SEM images of fractured surfaces of the (a) 'composite' developed on reduction aging at 1450 °C for 0 h and (b) nanocomposite developed on reduction aging for 20 h.

3.2. Wear resistance of the Al_2O_3–$FeAl_2O_4$ nanocomposites

3.2.1. Wear rates

A comparison of the abrasive wear rates for monolithic alumina, Al_2O_3–Fe_2O_3 solid solutions and the Al_2O_3–$FeAl_2O_4$ nanocomposites aged at 1450 °C is shown in Fig. 4a. The incorporation of Fe_2O_3 in solid solution resulted in a slight increase in the wear rate over that of monolithic Al_2O_3. Y_2O_3 doping did not affect the wear rates for either monolithic alumina or the solid solution to any notable degree. Aging for 0 h at 1450 °C resulted in only a small improvement in the wear resistance, even in the presence of Y_2O_3. The most important result of the present investigation is that the Al_2O_3–$FeAl_2O_4$ nanocomposites, developed on reduction aging of the Al_2O_3–Fe_2O_3 solid solutions for 10 and 20 h at 1450 °C, exhibited considerably reduced wear rates compared to Al_2O_3, the solid solutions and specimens with insufficient aging to develop intragranular nanoparticles. Additionally, doping with Y_2O_3 resulted in a further lowering of the wear rates for these nanocomposites. In the absence of Y_2O_3, the nanocomposite produced by aging for 10 h exhibited the lowest wear rate but with Y_2O_3-doping, the wear rate

Table 1
Vickers hardness (H_{V5}; GPa) for monolithic Al_2O_3, A10F solid solution and nanocomposites developed by reduction aging.

Materials	Y_2O_3-free	Y_2O_3-doped
Monolithic Al_2O_3 (as sintered; 1450 °C; 5 h)	20.1 ± 0.4	–
A10F solid solution (as sintered; 1450 °C; 5 h)	17.1 ± 0.8	16.9 ± 0.9

Aged samples	Aging temperature: 1450 °C		Aging temperature: 1550 °C	
	Y_2O_3-free	Y_2O_3-doped	Y_2O_3-free	Y_2O_3-doped
Al_2O_3–$FeAl_2O_4$ (aged in $N_2 + H_2$ for 0 h)	17.8 ± 0.3	17.4 ± 0.4	17.1 ± 0.4	17.2 ± 0.5
Al_2O_3–$FeAl_2O_4$ (aged in $N_2 + H_2$ for 10 h)	18.6 ± 0.2	18.9 ± 0.5	16.8 ± 0.2	17.1 ± 0.8
Al_2O_3–$FeAl_2O_4$ (aged in $N_2 + H_2$ for 20 h)	18.4 ± 0.7	19.1 ± 0.8	15.6 ± 1.9	15.9 ± 1.5

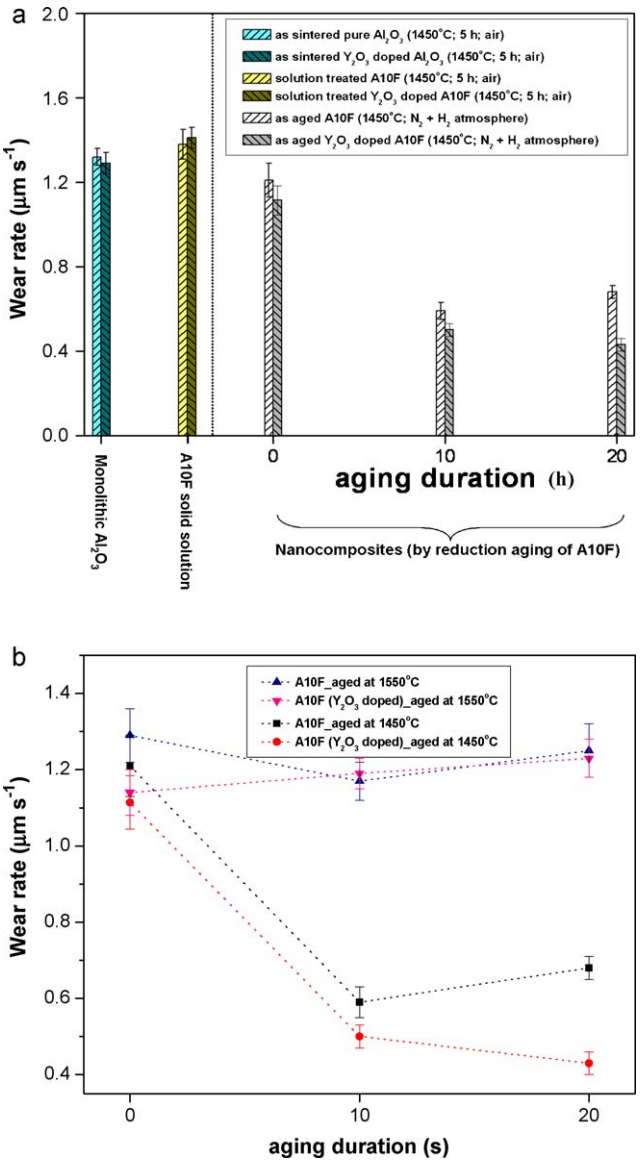

Fig. 4. (a) Abrasive wear rates against aging duration at 1450 °C for the Al_2O_3–$FeAl_2O_4$ nanocomposites. The wear rates measured for the monolithic alumina and the Al_2O_3–10 wt.% Fe_2O_3 solid solution are also presented for comparison. (b) Plot of abrasive wear rates against aging duration at 1450 °C and 1550 °C for the Al_2O_3–$FeAl_2O_4$ particulate nanocomposites.

decreased monotonically with increase in the aging duration up to 20 h. The wear rate of this Y_2O_3 doped specimen was lower by a factor of 1.6 than that of the corresponding Y_2O_3-free specimen, and by a factor of 2.8 compared with that of a monolithic alumina of similar grain size. This improvement in abrasive wear resistance for Al_2O_3–$FeAl_2O_4$ nanocomposites over that of monolithic Al_2O_3 approaches the maximum improvement (a factor of ~3.4) reported for Al_2O_3–SiC nanocomposites when measured using the same experimental procedure.[5,6]

Fig. 4b shows the wear rates obtained with the nanocomposites developed at the higher reduction aging temperature of 1550 °C along with the 1450 °C results for comparison. It is evident that the nanocomposites developed at the higher aging temperature possessed inferior wear resistance with respect to those aged at 1450 °C. Indeed, no significant reduction in the wear rates could be seen after aging at 1550 °C. For this aging temperature, Y_2O_3-doping improved the wear resistance only for the nanocomposite developed on aging for 0 h, and then only by a small amount.

3.2.2. Observation of the worn surfaces

In order to gain insight into the wear mechanisms, the worn surfaces were examined using SEM. The images corresponding to the worn surfaces of monolithic alumina, solid solution and the composites developed via reduction aging are presented in Figs. 5–7.

The worn surface of monolithic alumina showed the classical features of extensive pullout,[2,3,5,6] whereby large pieces of material are removed by brittle fracture (Fig. 5a). The average pullout diameter was 4.5 μm, which is larger than the Al_2O_3 grain size (3 μm). Such pullouts occupied an area fraction of 53% of the worn surface. Pullout formation was by intergranular fracture (inset of Fig. 5a). The worn surfaces of the A10F and A10FY solid solutions were also characterised by extensive pullout by intergranular fracture (Fig. 5b). Due to the extremely rough topography of these worn surfaces, with pullout accounting for nearly ~80% of the area, precise estimation of the pullout size could not be made.

Fig. 6 shows the worn surfaces of the nanocomposites developed on aging of A10F solid solutions (without Y_2O_3) at 1450 °C. The composite aged for 0 h (Fig. 6a), in which only

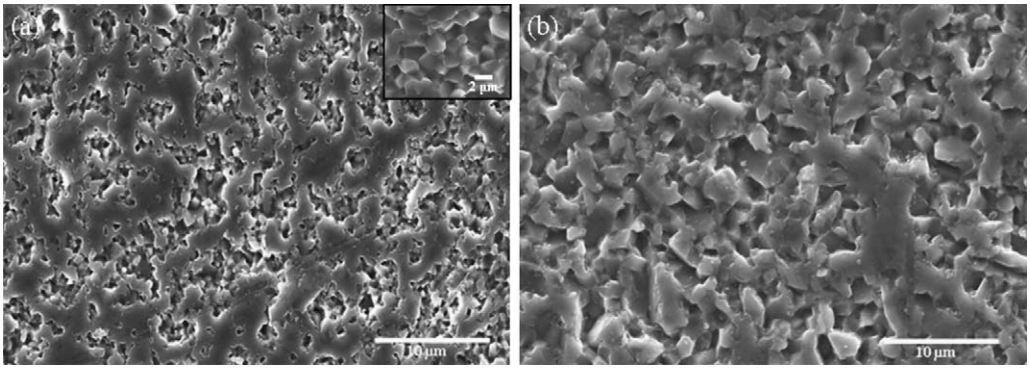

Fig. 5. SEM images of worn surfaces of (a) monolithic Al_2O_3 and (b) Al_2O_3–10 wt.% Fe_2O_3 (A10F) solid solution. Inset in (a) is a higher magnification view of one of the pullouts.

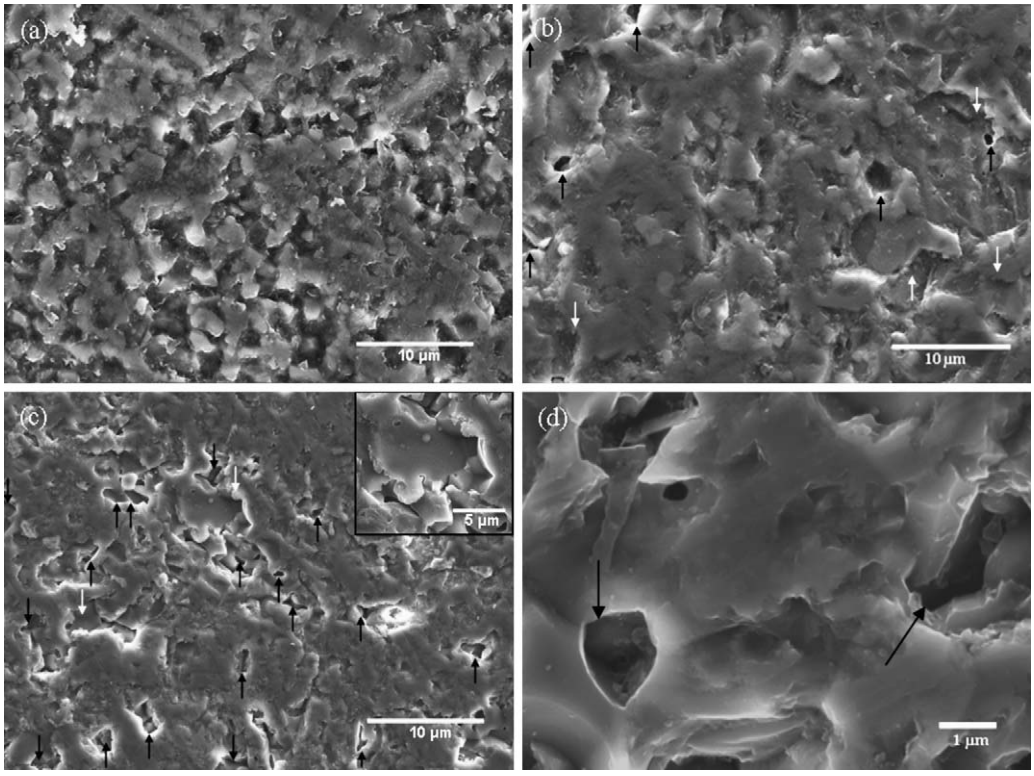

Fig. 6. SEM images obtained from the worn surfaces of the nanocomposites developed upon reduction aging of A10F at 1450 °C for (a) 0 h; (b) 10 h; (c) and (d) 20 h. The black and white arrows indicate two different types of pullout like features (see main text). Inset of (c) presents a higher magnification view of one of the large pullouts showing transgranular fracture.

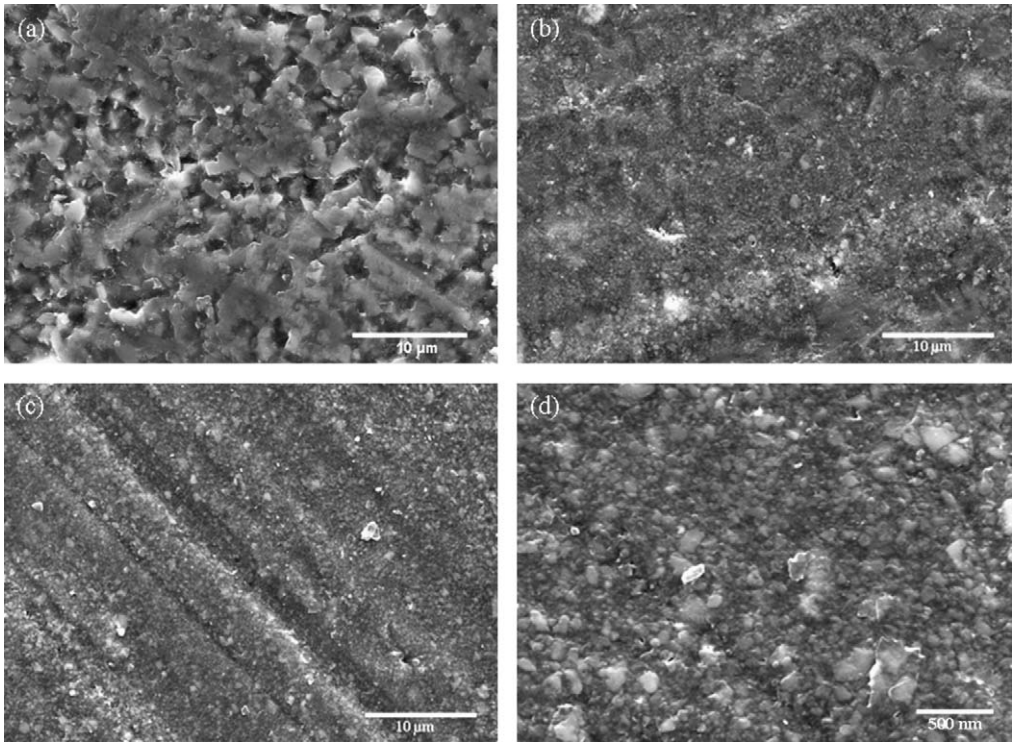

Fig. 7. SEM images obtained from the worn surfaces of the Y_2O_3-doped nanocomposites developed upon reduction aging of A10FY at 1450 °C for (a) 0 h; (b) 10 h; (c) and (d) 20 h. Note the almost complete absence of pullouts in (b) and (c).

grain boundary precipitates were present, suffered pullout by intergranular fracture similar to monolithic Al_2O_3 (Fig. 5a) and Al_2O_3–Fe_2O_3 solid solution (Fig. 5b). By contrast, the worn surfaces of the nanocomposites developed on aging for 10 h (Fig. 6b) and 20 h (Fig. 6c), in which nanosized intragranular particles had precipitated, developed much smoother worn surfaces with much less pullout. Careful observation reveals that the pullouts in these materials can be grouped into two types. One set of pullouts have dimensions between 1 and 2 μm (some indicated by black arrows in Fig. 6b–d) and appear to have been formed due to some of the coarse intergranular precipitates falling out during grinding, as can also be observed from the higher magnification image presented in Fig. 6d. The other set of pullouts (white arrows in Fig. 6b and c), are larger in dimensions (up to ~5 μm) and tend to be associated with transgranular fracture of the matrix grains (inset of Fig. 6c). It is apparent from Fig. 6b and c that the pullouts due to transgranular fracture occurred less frequently and are much shallower than the pullouts associated with the removal of the intergranular precipitates. Also, there are more of the latter (particle pullouts) in the specimen aged for 20 h than in the 10 h specimen.

The effect of Y_2O_3 doping on the appearance of the worn surfaces of the composites aged at 1450 °C is shown in Fig. 7. The surface of the specimen aged for 0 h (Fig. 7a) was similar to its Y_2O_3-free counterpart. However, the worn surfaces of the Y_2O_3-doped nanocomposites aged for 10 h (Fig. 7b) and 20 h (Fig. 7c) were almost completely devoid of pullouts of any kind; only abrasive scratches formed by plastic deformation can be observed on the worn surfaces.

Fig. 7b and c shows many surface particles, suggesting the presence of a compacted layer of wear debris. Observations at higher magnification suggest that such features are an inherent part of the structure of the worn surfaces (Fig. 7d). The formation of a tribolayer seems unlikely given the high material removal rates, however, and the absence of such a layer in the other specimens. In addition, a common feature of tribolayers is that new phases are formed due to tribochemical reactions, but no extra peaks were present in the X-ray diffraction (XRD) patterns taken from the worn surfaces (Fig. 8a). There was some broadening of the diffraction peaks of both phases present, however (Fig. 8b), which may be due to strain induced by plastic deformation. We conclude that any tribolayer was minimal and that the particles observed in the surface are simply the $FeAl_2O_4$ precipitates, made visible by atomic number contrast.

SEM images of the worn surfaces obtained with the nanocomposites aged at 1550 °C are shown in Fig. 9. The Y_2O_3-free composite aged for 0 h showed the presence of extensive pullouts caused by intergranular fracture (Fig. 9a) as for the 0 h/1450 °C composite. Extensive pullout persisted after aging for longer times at 1550 °C and was again by a mixture of transgranular fracture of matrix grains and more significantly due to fall out of the coarser second phase particles (Fig. 9b). Y_2O_3-doping did not have as much effect on the appearance of the worn surfaces of the nanocomposites aged at 1550 °C as on those aged at 1450 °C; there was still extensive pullout although the surface features were finer than those seen in the absence of Y_2O_3 (Fig. 9c and d).

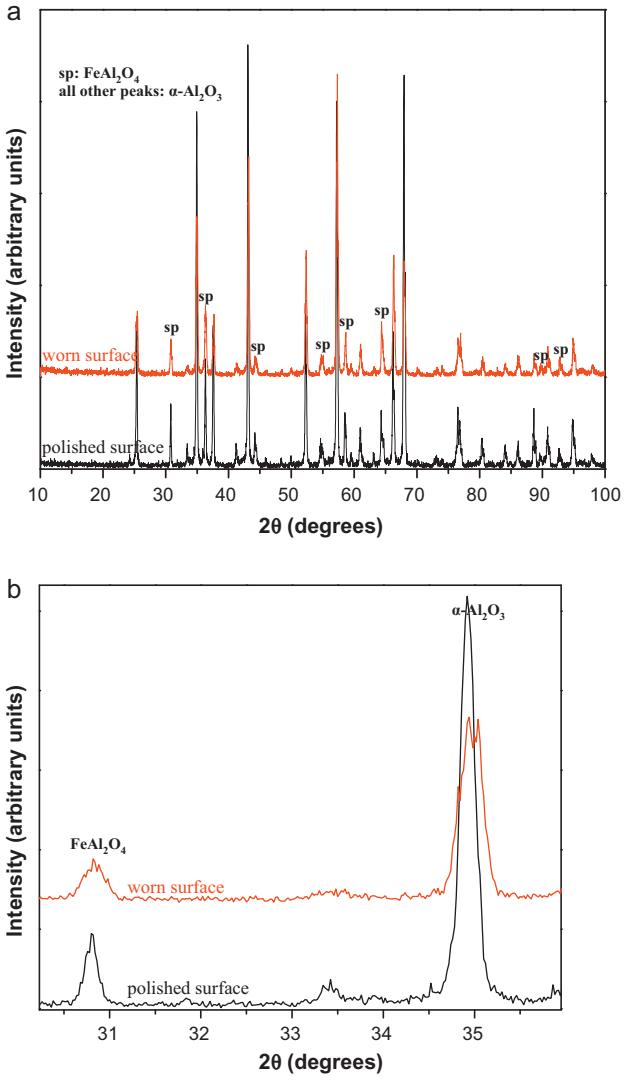

Fig. 8. (a) XRD patterns recorded from the polished and worn surfaces of nanocomposites developed by aging A10FY (~250 ppm Y_2O_3-doped Al_2O_3–10 wt.% Fe_2O_3 solid solutions) at 1450 °C for 20 h in reducing atmosphere (N_2 + 4% H_2); (b) magnified view of the $FeAl_2O_4$ and α-Al_2O_3 peaks showing peak broadening in the pattern obtained from the worn surface.

3.3. Indentation polish test

In order to investigate the subsurface damage caused by plastic deformation, the 1 μm diamond polished surfaces of previously indented specimens were examined in the SEM (see Section 2.2). Images after polishing to the bottom of the indentation are presented in Fig. 10, along with the original indentations before polishing. In the images of the polished indentations (Fig. 10b, d and f), the remaining parts of the original indentations can be seen in the centre of the picture, along with the traces of the classical radial cracks outside the indentation plastic zone. The boundaries of the original indentations are indicated by dashed lines. It is evident from the results for monolithic alumina (Fig. 10b) that whilst most of the surface has been well polished by the 1 μm diamond paste, a lot of surface pullouts occurred in a well-defined region corresponding closely to the shape and size of the original indentation before surface removal by

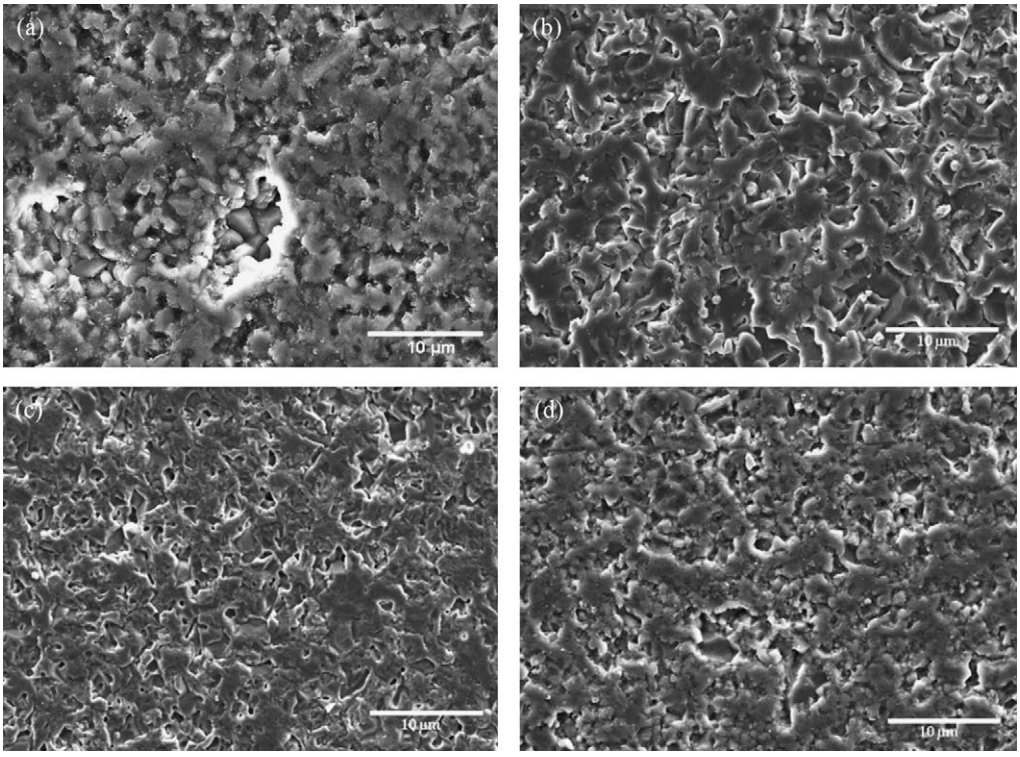

Fig. 9. SEM images obtained from the worn surfaces of the nanocomposites developed via reduction aging of A10F solid solutions at 1550 °C for (a) 0 h; (b) 20 h; and reduction aging of A10FY (∼250 ppm Y_2O_3-doped solid solutions) at 1550 °C for (c) 0 h and (d) 20 h.

subsequent polishing. This is assumed to be the plastic zone beneath the indentation. Similar pullouts can be seen in the indentation plastic zone of the A10F solid solution specimen (Fig. 10d). By contrast, although some pullout is evident over the whole surface, with much of it being due to the loss of coarse $FeAl_2O_4$ particles, the polished indentation plastic zone of the 20 h/1450 °C nanocomposite does not show a significantly higher level of pullout (Fig. 10f) than the surrounding material. This suppression of fracture initiation in the indentation plastic zone has been observed previously in Al_2O_3–SiC nanocomposites.[6]

4. Discussion

The results show that the aging schedule and consequent microstructural development has an enormous effect on the wear behaviour of the $Al_2O_3/Fe_2O_3/FeAl_2O_4$ ceramics. The main conclusions are (i) that Fe^{3+} in solid solution in Al_2O_3 leads to a modest reduction in hardness and wear resistance compared with pure alumina, (ii) the presence of nanoscale $FeAl_2O_4$ precipitates within the grains has a very beneficial effect on the wear resistance of the materials, and (iii) coarse $FeAl_2O_4$ particles at the alumina grain boundaries tend to fall out of the surface, thus reducing the wear resistance. The reduction of hardness of Al_2O_3 caused by Fe_2O_3 in solid solution is well known[20] and the general correlation between hardness and wear resistance is sufficient to explain the present results. The influence of the precipitation of $FeAl_2O_4$ particles will now be explored in more detail.

4.1. Influence of nanosized intragranular $FeAl_2O_4$ precipitates on wear

The presence of nanosized $FeAl_2O_4$ precipitates appears to have a similar effect on wear resistance to that observed with SiC,[5–7] that is the wear rate is reduced by a factor ∼3 compared with pure Al_2O_3, even though in the present case the hardness of these aged materials is slightly less than that of Al_2O_3. The improvements in the Al_2O_3/SiC system have been shown to have two sources.[5,6] The first is the change in fracture mode from intergranular to transgranular on adding the SiC, which results in a reduction in size of each individual pullout resulting from the initiation of a surface or near-surface crack.[5] The second is that intragranular SiC particles are thought to block the twins and/or dislocation pileups thought to be responsible for nucleating the near-surface cracking during grinding.[6]

Considering the fracture mode first, the same change in fracture mode is observed in the current $Al_2O_3/FeAl_2O_4$ composites (Fig. 3, Section 3.1) as in the Al_2O_3/SiC system and can therefore be safely assumed to make a major contribution to the reduction in wear rate on formation of the nanosized precipitates within the grains. The reason for the change in fracture mode in this case is not clear however. In the alumina/SiC system, there is persuasive evidence that SiC nanoparticles on the grain boundaries can deflect intergranular cracks into the grain interior because of a mixture of compressive residual stresses in the particles, high particle and good particle–matrix bonding, all of which hinder the passage of the crack past the grain boundary particle.[21,22] The change in fracture mode is also seen with relatively low volume fractions of coarse SiC, however, and it has

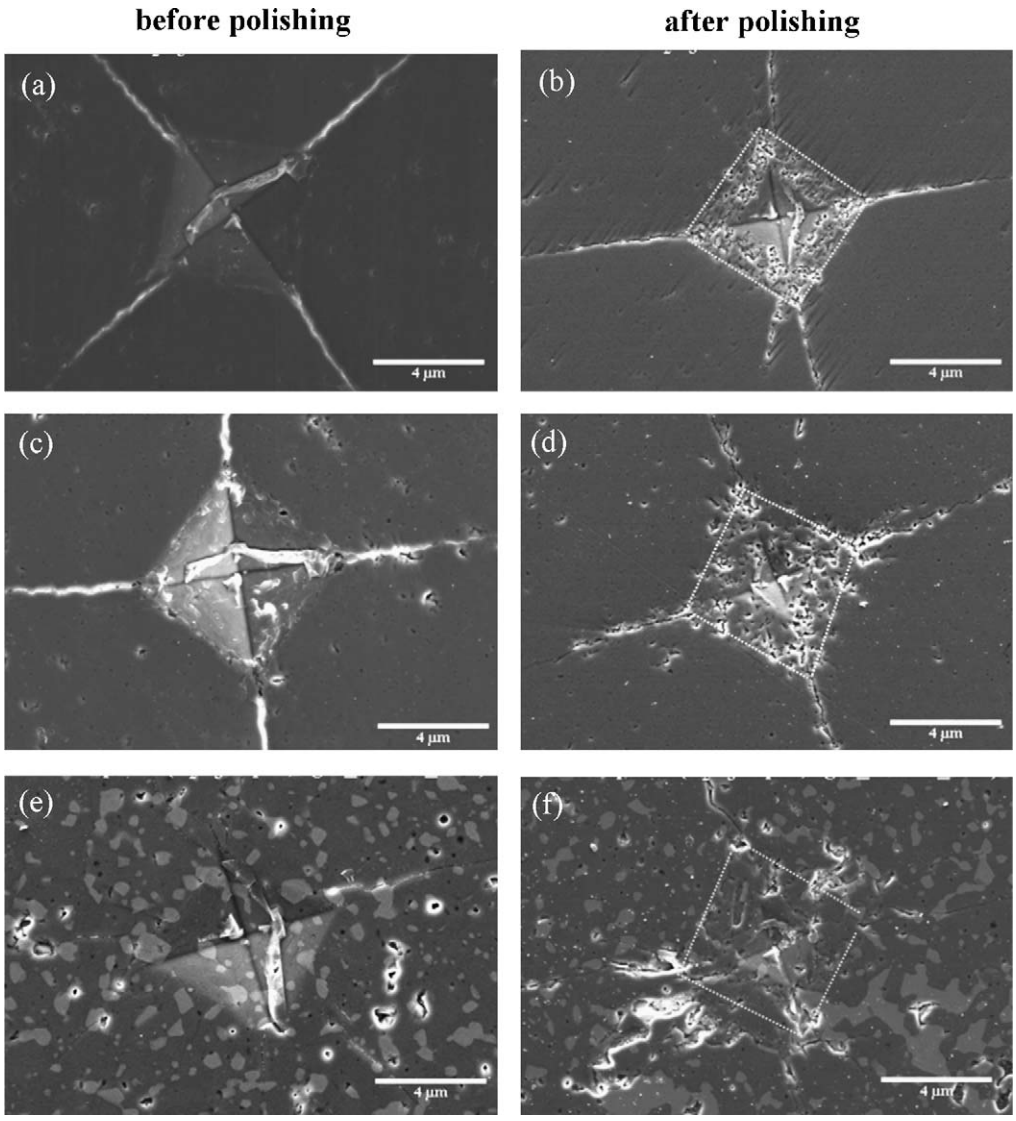

Fig. 10. SEM images of the original indentations (10 kg) and the partly polished remnant indentations (1 μm diamond paste), respectively, obtained on (a) and (b) monolithic Al_2O_3; (c) and (d) A10F solid solution; (e) and (f) nanocomposite developed on aging A10F for 20 h at 1450 °C. Note the presence of extensive cracking induced pullout in the indentation plastic zones of the monolithic alumina and A10F solid solutions, but very little plasticity induced damage in the nanocomposites.

been argued that impurities, possibly carbon, introduced with the SiC also play a role by strengthening the grain boundaries.[6,23] In the present materials, however, none of these factors can be responsible for the change in fracture mode: the change in fracture mode only becomes significant when nanoparticles appear within the grains rather than grain boundary particles being involved, there are very few fine particles on the grain boundaries in any of the microstructures and in any case the particles are less stiff than alumina, have a thermal expansion greater than that of alumina so that they are in tension rather than compression (see below) and are not well bonded to the alumina (Figs. 1d and 2a). Although impurity segregation to the grain boundaries has not been studied in these materials, it is difficult to see why this would differ significantly between the composite reduction aged for "0 h", in which grain boundary particles of $FeAl_2O_4$ have already been produced and the main fracture mode remains intergranular, and the specimens aged for ≥10 h, where predominantly transgranular fracture occurred. The only obvious differences between these specimens are the appearance of the intragranular particles and a coarsening of the grain boundary particles. It is evident that further investigation is needed in this area.

Turning now to the other mechanism for improved wear resistance known from the Al_2O_3/SiC system, crack initiation may be hindered because the intragranular nanoparticles impede twinning and dislocation motion during the surface plastic deformation caused by grinding.[6] Plastic deformation still occurs but the length of the associated deformation bands is limited to the distance between the particles so that the stress concentration at the head of any individual band is no longer sufficient to nucleate a crack. The experimental results in the present materials appear very similar to those from Al_2O_3/SiC nanocomposites and offer plenty of support for this mechanism. The presence of pulledout material because of microcracking in the plastic zones of indentations in pure alumina and solid solutions (Fig. 10) shows that plasticity is indeed a potent source of crack initiation. The suppression of microcracking in the plastic zone

of hardness indentations is clear (Fig. 10) and occurred only when the aging treatment produces intragranular nanoparticles of $FeAl_2O_4$, as did the improvements in wear resistance. Furthermore, direct evidence of the proposed interactions between twins/dislocations and the intragranular particles was found during TEM investigation of fractured bend specimens of the nanocomposites developed at 1450 °C for 20 h. There were many apparent interactions of the intragranular particles with dislocations (Fig. 11a and b). Fig. 11c shows clear evidence that twins were blocked by the $FeAl_2O_4$ particles within the alumina grains, whereas the majority of twins in pure Al_2O_3 extended right across the grains from one grain boundary to the other (Fig. 11d).

4.2. *Influence of coarse grain boundary $FeAl_2O_4$ precipitates on wear*

The worn surfaces of the nanocomposites show pullouts occurring due to the falling out of the coarser, micron scale second phase particles, which were mostly present along the matrix grain boundaries (Figs. 6 and 9b–d). The frequency of occurrence of such pullouts increased with the increase in aging

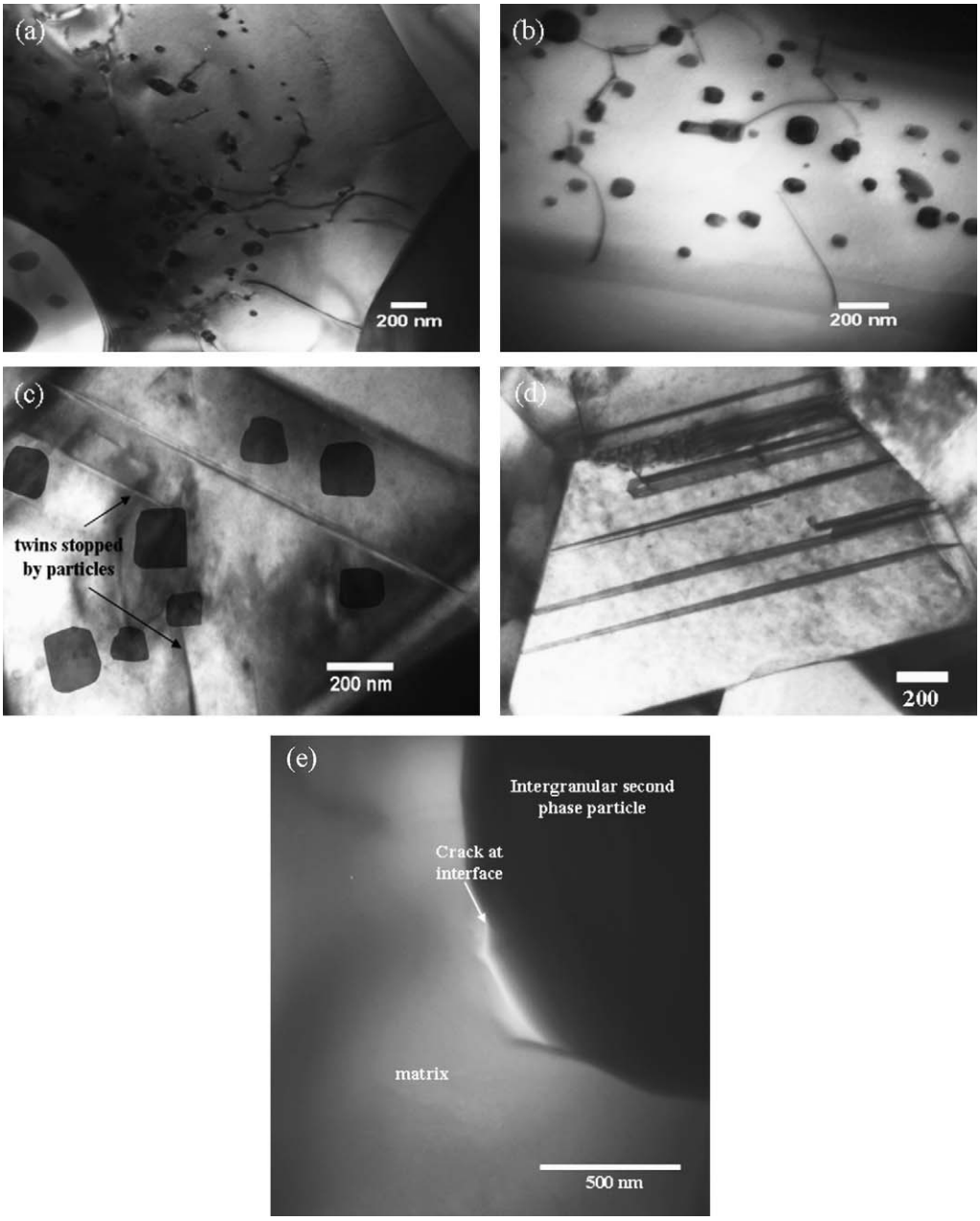

Fig. 11. Bright field TEM images showing (a–c) interaction of deformation bands (dislocations and twins) with intragranular nanosized particles in foil obtained from the tensile surface of bent bar of Al_2O_3–$FeAl_2O_4$ nanocomposites, developed by reduction aging of A10F at 1450 °C for 20 h; (d) twins propagating unhindered from one grain boundary to another in a foil obtained from the tensile surface of bent bar of monolithic Al_2O_3; (e) presence of crack at the interface of an intergranular particle with the matrix (A10F aged 20 h at 1450 °C).

duration and temperature, which in turn is correlated with the increase in average size of these particles. The coarse particles present in the nanocomposites aged for 20 h, have also been observed to fall out during preparation of TEM samples (see Fig. 2b) and to fracture during bend tests.[12,13] By contrast, the nanosized intragranular particles have rarely been observed to fall out in any of the processes.

Since the thermal expansion co-efficients of the matrix (Al_2O_3; $\alpha_m \sim 8 \times 10^{-6}\,K^{-1}$ [24,25]) and the second phase particles ($FeAl_2O_4$; $\alpha_p \sim 13 \times 10^{-6}\,K^{-1}$ [25]) are different, stresses will develop in the two phases during cooling from the heat treatment temperatures. In the present case the radial stress at the particle/matrix interface is expected to be tensile and this can effectively weaken the particle/matrix interfaces and even lead to spontaneous circumferential cracking around the interfaces above a certain critical size of the second phase particles.[26–29] For low volume fractions of particles, the pressure (P) which the particles are subjected to during cooling from the heat treatment temperatures can be approximately estimated from the following expression developed by Weyl[30] and Selsing[31]:

$$P = \frac{\Delta\alpha\Delta T}{(1+\nu_m)/2E_m + (1-2\nu_p)/E_p} \quad (2)$$

In this equation, $\Delta\alpha = \alpha_m - \alpha_p \sim -5 \times 10^{-6}\,K^{-1}$, ΔT is the cooling range over which plasticity is considered to be negligible ~1000 °C, ν_m and E_m are the Poisson's ratio (~0.2) and elastic modulus (~350 GPa) of the matrix (Al_2O_3),[32] ν_p and E_p are the Poisson's ratio (~0.3) and elastic modulus (~225 GPa) of the second phase particles ($FeAl_2O_4$).[33,34] Eq. (1) gives a value of −1.4 GPa for the pressure (P) which the particles are subjected to (i.e. the stress is tensile).

Based on an energy balance criterion, Davidge and Green[26] developed the following expression for the critical radius of the second phase particles (R_c), above which spontaneous cracking is possible due to the pressure (P) developed during cooling from the fabrication/heat treatment temperature:

$$R_c = \frac{8\gamma_s}{P^2\{(1+\nu_m)/E_m + 2(1-2\nu_p)/E_p\}} \quad (3)$$

where γ_s is the effective surface energy at the particle matrix interface. Assuming a toughness of ~1 MPa $m^{1/2}$ for the interface and using the mean of the Young's moduli of Al_2O_3 and $FeAl_2O_4$ allows γ_s to be estimated as $G_c/2 \sim 2\,J/m^2$ giving a value of 1 μm for R_c. This indicates that second phase particles of sizes greater than ~2 μm are liable to develop spontaneous cracks along their interfaces with the matrix.

This critical size for spontaneous cracking explains several details of the results. It correctly predicts that the nanosized particles should be free from any cracking along the interface, whilst the coarser micron scale intergranular secondary phase particles are more prone towards peripheral cracking. The presence of microcracks along the interface of the coarse particles was observed during TEM investigations (Fig. 11e). The microcracking leads to the pullout of the coarse particles during wear of the nanocomposites. After aging for 10 h at 1450 °C, the mean particle size was just below the critical size (see Section 3.1) so the consequences are not severe and the reduction in size of the grain boundary particles on doping with Y_2O_3 resulted in only a slight reduction in wear rate (Fig. 4). After aging for 20 h at 1450 °C, however, the intergranular particle size in the absence of Y_2O_3 exceeds 2 μm and it is reasonable to suppose that this is responsible for the small increase in wear rate compared with the 10 h specimen seen in Fig. 4. The particle size in the Y_2O_3 doped specimen aged for 20 h at 1450 °C remains close to 1 μm, however, so the further development of the nanoparticles with the increased aging time is able to yield further improvements in wear resistance. Finally, in all the nanocomposites developed at 1550 °C the average sizes of the intergranular particles are well in excess of the critical size, irrespective of the absence or presence of Y_2O_3. The particles therefore fall out spontaneously from the surface of the composite. This, and the fact that the nano-precipitate free zones close to the grain boundaries are wider after aging at this higher temperature[12] are thought to be the reasons why the composites aged at 1550 °C did not show improved wear resistance compared with alumina.

5. Conclusions

The abrasive wear resistance of "in situ" $Al_2O_3/FeAl_2O_4$ nanocomposites produced by the aging of Al_2O_3–10 wt% Fe_2O_3 solid solutions in a reducing atmosphere has been investigated, with the following conclusions.

(a) Al_2O_3–$FeAl_2O_4$ nanocomposites could be produced with wear resistance improved by almost a factor of 3 compared with pure alumina of the same grain size.
(b) Optimising the wear resistance is a matter of maximising the precipitation of nanosized particles of $FeAl_2O_4$ within the grains and minimising both the volume fraction and size of the coarser grain boundary precipitates.
(c) The nanosized particles within the grains improved the wear resistance by inhibiting crack initiation by deformation bands during grinding and reducing the size of the individual surface pullouts by changing the fracture mode from intergranular in pure alumina to transgranular in the nanocomposites.
(d) Tensile thermal stresses around coarse grain boundary particles led to spontaneous cracking when their size exceeded ~2 μm. The resulting falling out of the particles from the surface during wear was the main source of their detrimental effect.
(e) The optimum microstructure was produced by reduction aging of solid solutions doped with 250 ppm Y_2O_3 for 10–20 h at 1450 °C. The Y_2O_3 inhibited the growth of the grain boundary precipitates by reducing the grain boundary diffusion coefficients.

References

1. Niihara K. New design concept of structural ceramics—ceramic nanocomposites. *J Ceram Soc Jpn* 1991;**99**(10):974–82 [The Centennial Memorial Issue].

2. Mukhopadhyay A, Basu B. Consolidation-microstructure-property relationships in bulk nanoceramics and ceramic nanocomposites: a review. *Int Mater Rev* 2007;**52**(5):257–88.
3. Mukhopadhyay A. Tribological properties and processing challenges of bulk structural ceramic nanomaterials. *Tribol – Mater Surf Interfaces* 2008;**2**(3):169–84.
4. Sternitzke M. Review: structural ceramic nanocomposites. *J Eur Ceram Soc* 1997;**17**:1061–82.
5. Ortiz Merino JL, Todd RI. Relationship between wear rate, surface pull-out and microstructure during abrasive wear of alumina and alumina/SiC nanocomposites. *Acta Mater* 2005;**53**:3345–57.
6. Limpichaipanit A, Todd RI. The relationship between microstructure, fracture and abrasive wear in Al_2O_3/SiC nanocomposites and microcomposites containing 5 and 10% SiC. *J Eur Ceram Soc* 2009;**29**:2841–8.
7. Walker CN, Borsa CE, Todd RI, Davidge RW, Brook RJ. Fabrication, characterisation and properties of alumina matrix nanocomposites. *Br Ceram Proc* 1994;**53**:249–64.
8. Zhao J, Stearns LC, Harmer MP, Chan HM, Miller GA, Cook RF. Mechanical behavior of alumina–silicon carbide nanocomposites. *J Am Ceram Soc* 1993;**76**:503–10.
9. Stearns LC, Zhao J, Harmer MP. Processing and microstructure development in Al_2O_3–SiC 'nanocomposites'. *J Eur Ceram Soc* 1992;**10**: 473–7.
10. Jeong YK, Nakahira A, Niihara K. Effects of additives on microstructure and properties of alumina–silicon carbide nanocomposites. *J Am Ceram Soc* 1999;**92**:3609–12.
11. Cock AM, Shapiro IP, Todd RI, Roberts SG. Effects of yttrium on the sintering and microstructure of alumina–silicon carbide "nanocomposites". *J Am Ceram Soc* 2005;**88**:2354–61.
12. Mukhopadhyay A, Todd RI. Microstructure and mechanical properties of Al_2O_3 matrix nanocomposites developed via solid state precipitation. *J Eur Ceram Soc* 2010;**30**:1359–72.
13. Mukhopadhyay A, Todd: RI. Effect of yttria doping on the microstructure and mechanical properties of Al_2O_3–$FeAl_2O_4$ nanocomposites developed via solid state precipitation. *J Eur Ceram Soc* 2010;**30**: 2905–15.
14. Mukhopadhyay A, Todd RI. Production of Alumina matrix nanocomposites by solid state precipitation. In: Mathur S, Singh M, Singh D, Salem J, editors. *Nanostructured Materials and Nanotechnology III, Ceramic Engineering and Science Proceedings 30(7)*. 2010. p. 119–31.
15. Ou U, Japanese Patent 3340025, special publication 09-328355 1997.
16. Coble RL. Sintering crystalline solids. II. Experimental test of diffusion models in powder compacts. *J Appl Phys* 1961;**32**(5):793–9.
17. Korinek SL, Carry C, Priester L. Multiscale aspects of the influence of yttrium on microstructure, sintering and creep of alumina. *J Eur Ceram Soc* 2002;**22**:1525–41.
18. Lartigue S, Carry C, Priester L. Grain boundaries in high temperature deformation of yttria and magnesia co-doped alumina. *J Phys (Paris), C1* 1990;**51**:985–90.
19. Cho J, Harmer MP, Chan HM, Rickman JM, Thompson AM. Effect of yttrium and lanthanum on the tensile creep behavior of aluminium oxide. *J Am Ceram Soc* 1997;**80**(4):1013–7.
20. Kennedy CR, Bradt RC. Softening of Al_2O_3 by solid solution of $MgO{\cdot}TiO_2$. *J Am Ceram Soc* 1973;**56**:608–1608.
21. Jiao S, Jenkins ML, Davidge RW. Electron microscopy of crack/particle intersections in Al_2O_3/SiC nanocomposites. *J Microsc* 1997;**185**(2):259–64.
22. Jiao S, Jenkins ML, Davidge RW. Interfacial fracture energy–mechanical behaviour relationship in Al_2O_3/SiC and Al_2O_3/TiN nanocomposites. *Acta Mater* 1997;**45**(1):149–56.
23. Marquis EA, Yahya NA, Larson DJ, Miller MK, Todd RI. Probing the improbable: imaging carbon atoms in alumina. *Mater Today* 2010;**13**:34–6.
24. Ishizawa N, Miyata T, Minato I, Marumo F, Iwai S. A structural investigation of α-Al_2O_3 at 2170 K. *Acta Crystallogr Sect B: Struct Sci* 1980;**36**:228–30.
25. Fujimura T, Tanaka SI. In-situ high temperature X-ray diffraction study of Fe/Al_2O_3 interface reactions. *J Mater Sci* 1999;**34**:425–9.
26. Davidge RW, Green TJ. The strength of two-phase ceramic/glass materials. *J Mater Sci* 1968;**3**:629–34.
27. Rice RW, Pohanka RC. Grain-size dependence of spontaneous cracking in ceramics. *J Am Ceram Soc* 1979;**62**:559–63.
28. Mukhopadhyay A, Raju GB, Basu B, Suri AK. Correlation between phase evolution, mechanical properties and instrumented indentation response of TiB_2-based ceramics. *J Eur Ceram Soc* 2009;**29**:505–16.
29. Evans AG. The role of inclusions in the fracture of ceramic materials. *J Mater Sci* 1974;**9**:1145–52.
30. Weyl D. Influence of internal strains on the texture and mechanical strength of porcelains. *Ber Deut Keram Ges* 1959;**36**:319–24.
31. Selsing J. Internal stresses in Ceramics. *J Am Ceram Soc* 1961;**44**:419.
32. Munro RG. Elastic moduli data for polycrystalline ceramics. *NISTIR* 2002;**6853**. Gaithersburg, Maryland 20899.
33. Reichmann HJ, Jacobsen SD. Sound velocities and elastic constants of $ZnAl_2O_4$ spinel and implications for spinel-elasticity systematics. *Am Mineral* 2006;**91**:1049–54.
34. Wang H, Simmons G. Elasticity of some mantle crystal structures 1. Pleonaste and hercynite spinel. *J Geol Res* 1972;**77**:4379–92.